Monthly Notices
of the
ROYAL ASTRONOMICAL SOCIETY

MNRAS **508,** 1459–1472 (2021)
Advance Access publication 2021 September 11

https://doi.org/10.1093/mnras/stab2580

Resolving local and global kinematic signatures of satellite mergers with billion particle simulations

Jason A. S. Hunt,[1]★ Ioana A. Stelea,[2] Kathryn V. Johnston,[1,2] Suroor S. Gandhi,[3]
Chervin F. P. Laporte[4,5] and Jeroen Bédorf[6]

[1] *Center for Computational Astrophysics, Flatiron Institute, 162 5th Avenue, New York City, NY 10010, USA*
[2] *Department of Astronomy, Columbia University, New York, NY 10027, USA*
[3] *Center for Cosmology and Particle Physics, Department of Physics, New York University, 726 Broadway, New York, NY 10003, USA*
[4] *Institut de Ciències del Cosmos (ICCUB), Universitat de Barcelona (IEEC-UB), Martí i Franquès 1, E-08028 Barcelona, Spain*
[5] *Kavli Institute for the Physics and Mathematics of the Universe (WPI), The University of Tokyo Institutes for Advanced Study (UTIAS), The University of Tokyo, Chiba 277-8583, Japan*
[6] *Leiden Observatory, Leiden University, P.O. Box 9513, NL-2300 RA Leiden, the Netherlands*

Accepted 2021 September 8. Received 2021 September 6; in original form 2021 June 30

ABSTRACT

In this work, we present two new $\sim 10^9$ particle self-consistent simulations of the merger of a Sagittarius-like dwarf galaxy with a Milky Way (MW)-like disc galaxy. One model is a violent merger creating a thick disc, and a *Gaia*–Enceladus/Sausage-like remnant. The other is a highly stable disc which we use to illustrate how the improved phase space resolution allows us to better examine the formation and evolution of structures that have been observed in small, local volumes in the MW, such as the $z - v_z$ phase spiral and clustering in the $v_R - v_\phi$ plane when compared to previous works. The local $z - v_z$ phase spirals are clearly linked to the global asymmetry across the disc: we find both 2-armed and 1-armed phase spirals, which are related to breathing and bending behaviours, respectively. Hercules-like moving groups are common, clustered in $v_R - v_\phi$ in local data samples in the simulation. These groups migrate outwards from the inner galaxy, matching observed metallicity trends even in the absence of a galactic bar. We currently release the best-fitting 'present-day' merger snapshots along with the unperturbed galaxies for comparison.

Key words: Galaxy: disc – Galaxy: kinematics and dynamics – solar neighbourhood – Galaxy: structure.

1 INTRODUCTION

The Milky Way (MW) has long been known to be a barred spiral galaxy (e.g. Blitz & Spergel 1991), but our location within it leads to complex observational selection effects such as those imposed by the dust extinction, which make it difficult to construct a global picture of our home galaxy. Thus, the observational data has long been complemented by the construction of various MW models, to help us understand the observational biases and reveal the Galaxy beyond. However, such modelling frequently assumes that the system is in equilibrium, which is a necessary (or significantly simplifying) assumption for many modelling techniques.

The second data release (DR2; Gaia Collaboration 2018) from the European Space Agency's *Gaia* mission (Gaia Collaboration 2016) highlighted just how far out of equilibrium our Galaxy is. For example, Antoja et al. (2018) showed for the first time the striking spiral, or snail shaped pattern in the $z - v_z$ plane, henceforth phase spiral. This phase spiral has been proposed to arise from the interaction of the MW with the Sagittarius dwarf galaxy, henceforth Sgr (e.g. Antoja et al. 2018; Khanna et al. 2019; Laporte et al. 2019). However, Bennett & Bovy (2021) find that the amplitude and wavelength of the vertical asymmetry in the Solar neighbourhood cannot be produced by Sgr alone, for a variety of MW potentials, and Sgr orbits and masses. One alternative is that the phase spiral can be created by the buckling of the Galactic bar (Khoperskov et al. 2019), although the lack of an age dependence in the phase spiral argues against this origin (Laporte et al. 2019).

Gaia DR2 also revealed ridge-like structures in the $R - v_\phi$ plane (Antoja et al. 2018; Kawata et al. 2018; Ramos, Antoja & Figueras 2018), an extension of the long known structure in local velocity space across several kpc. The ridges in the $R - v_\phi$ plane, or the local $v_R - v_\phi$ plane can be explained by bar resonances (e.g. Fragkoudi et al. 2019), spiral structure (e.g. Hunt et al. 2018), or the influence of an external perturber such as Sgr (e.g. Khanna et al. 2019; Laporte et al. 2019). The true cause is likely a complex combination of the three, which is non-trivial to disentangle.

To model the phase spiral, Binney & Schönrich (2018) employ a simple impulse approximation model of a satellite passing vertically through the galactic disc and reproduce a qualitatively similar phase spiral to that seen in the *Gaia* data, for an impact 400 ± 150 Myr ago, which could correspond to the previous pericentric passage of Sgr (Dierickx & Loeb 2017). However, as they are careful to note, this neglects both the geometry of the orbit and perturbation of the frequencies by the impactor. Binney & Schönrich (2018) also note that to reach the same resolution of the phase spirals

---

★ E-mail: jhunt@flatironinstitute.org

Published by Oxford University Press on behalf of Royal Astronomical Society

in a particle-based simulation $\geq 2 \times 10^8$ disc particles would be required, which would be computationally expensive in a fully self-consistent simulation, especially when also modelling the dark matter halo.

Such fully self-consistent merger simulations (e.g. Laporte et al. 2018b) better capture the real physics of such an interaction, with a dynamically consistent orbit, including dynamical friction and satellite mass-loss, along with an extended density profile for the satellite. Such models can reproduce large-scale disc dynamics and local kinematic features similar to those observed in the MW (e.g. Laporte et al. 2019), but lack the particle resolution to distinguish fine detail over a local volume at a level comparable to current data sets. Bland-Hawthorn & Tepper-García (2021) make a compromise by subjecting a live 7.45×10^7 particle galaxy to a point mass perturber, and find a complex response in the disc, consisting of the superposition of a density wave and a corrugated bending wave, which wrap at different rates, giving rise to phase spirals that last for multiple Gyr. However, even the 5×10^7 particles in their disc leaves the simulation on the edge of resolving fine features in the outer disc.

In particular, this is the part of the galaxy which will be heavily affected by interaction with a satellite (e.g. Kazantzidis et al. 2009; Gómez et al. 2017) which is also becoming increasingly accessible to observed data sets (e.g. Gaia Collaboration 2021; Laporte, Koposov & Belokurov 2021). Due to the longer orbital time-scales in the outer disc, older excited structures from prior interactions can remain coherent to the present day. For example, Laporte et al. (2020) confirmed the Anticenter stream (Grillmair 2006) to be a fossil relic of a past satellite interaction due to its large composition of predominantly old low-α stars when compared to the bulk of the disc at similar distances. Such mergers have important implications for the growth rate of the Galactic disc and its chemical evolution, making relics from past satellite interactions sensitive probes of the formation history of the Galaxy.

Currently, one of the limiting factors in our interpretation of simulations on local scales is the particle resolution. While the global signatures in such simulations can be easily resolved (e.g. Laporte et al. 2018b; Bland-Hawthorn & Tepper-García 2021), performing analyses of projections such as the $v_\mathrm{R}-v_\phi$ plane or the $z-v_z$ plane is difficult without increasing the volume of the 'local' sample, which in turn dilutes the signal. With *Gaia* DR2 we have entered a new regime where we have significantly more stars within a few hundred parsecs, with excellent astrometry and radial velocities, than are present in the same volume in the current generation of simulations.

While it is not currently feasible to construct models with the same number of particles as there are stars in our Galaxy, if we desire to improve local phase space resolution we have some options which enable us to get closer. First, we can use test particle simulations which require a fraction of the computational cost and enable us to precisely set the galactic parameters, but lack realistic gravitational dynamics. Secondly, we can use GPU accelerated *N*-body codes, such as `Bonsai` (Bédorf, Gaburov & Portegies Zwart 2012), which has achieved a 242 billion particle MW model while continuing to scale well (Bédorf et al. 2014). Other options would include 'Hybrid' simulations which add test particles to a self-consistent model (e.g. Quillen et al. 2011) to increase phase space resolution, but not the force resolution, or the use of the basis function expansion technique (e.g. Clutton-Brock 1972; Weinberg 1999) where the force calculation time-scales with $\mathcal{O}(N)$, instead of the $\mathcal{O}(N \log N)$ of tree codes, and retains comparable or superior force resolution (Petersen, Weinberg & Katz 2021). More realistic models which include gas, star formation and feedback further increase the computational cost, and are thus by necessity lower resolution than can be attained by pure *N*-body simulations regardless of the simulation technique. However, recent cosmological zoom simulations are achieving impressive resolutions, e.g. Grand et al. (2021) re-simulate a galaxy from the `Auriga` cosmological simulation (Grand et al. 2017) with $\sim 10^8$ stellar particles in the main MW-like galaxy.

In this work, we concern ourselves less with matching the MW–Sgr system, and more on resolving the response of a self-gravitating disc to a satellite perturber. Thus, we present high-resolution ($>1 \times 10^9$ particle) self-consistent simulations of two mergers, each between a MW-like disc galaxy and a dwarf, evolved with `Bonsai`, which pass the 2×10^8 disc particle threshold suggested by Binney & Schönrich (2018). We use them to illustrate local dynamical signatures that would be missed in lower resolution models. They are available online at Flathub,[1] and this paper serves as the reference document for the simulations, along with a brief analysis of the disc dynamics. In Section 2, we describe the setup of the simulations. In Section 3, we examine the structure and dynamics of the first galaxy, focusing on the $z-v_z$ phase spiral in Sections 3.2 and 3.3, and the planar dynamics in Section 3.4. In Section 4, we examine the second merger simulation. In Section 5, we give our conclusions.

2 THE SIMULATIONS

In this section, we describe the setup and evolution of the MW-like disc galaxies which we use as the host galaxies for the merger simulations, the satellite used for the merger, and their combination.

2.1 The isolated host galaxy simulations, Models D1 and D2

The initial conditions for the MW-like host galaxies, Models D1 and D2 were created with the parallelized version of the `galactics` initial condition generator[2] (Kuijken & Dubinski 1995). We chose to use the parameters from the MWa and MWb MW-like models from Widrow & Dubinski (2005), which are summarized in Table 1 as they are already well explored and the purpose of the paper is to examine the merger-driven structure and kinematics, not the construction of new best-fitting MW-like disc galaxies.

Model D1 (MWb in Widrow & Dubinski 2005) is a disc with a high Toomre parameter $Q = 2.3$ (Toomre 1964) which is stable against bar and spiral formation for several Gyr. While such a high stability disc is not representative of the MW, we consider it ideal when constructing a model in which the only non-axisymmetric structure and kinematics will form from interactions with the perturbing dwarf. For comparison, Model D2 (MWa in Widrow & Dubinski 2005) has a heavier disc and $Q = 1.3$, leaving it stable, but not unreasonably so (see Widrow & Dubinski 2005, for a detailed analysis of the models as isolated discs).

We use the GPU based *N*-body tree code `Bonsai` (Bédorf et al. 2012, 2014) to evolve Models D1 and D2 for ~ 5 Gyr, using a smoothing length of 50 pc and an opening angle $\theta_\mathrm{o} = 0.4$ radians. Table 2 shows the particle numbers and mass resolution per component for the models. While ideally we would like to have the same mass resolution in each component to avoid heating concerns, we are memory limited to around 1.3×10^9 particles on our current system, and we prioritize having at least 2×10^8 particles in the disc to increase local phase space resolution.

---

[1] https://flathub.flatironinstitute.org/jhunt2021

[2] https://github.com/treecode/galactics.parallel

Table 1. Halo tidal radius $\epsilon_{\rm h}$, halo characteristic velocity $\sigma_{\rm h}$, halo scale length $a_{\rm h}$, disc mass $M_{\rm d}$, disc scale length $R_{\rm d}$, disc scale height $h_{\rm d}$, bulge tidal radius $\epsilon_{\rm b}$, characteristic bulge velocity $\sigma_{\rm b}$, bulge scale length $a_{\rm b}$, and Toomre parameter Q for the MW-like disc galaxy initial conditions for the `galactics` initial condition generator, as taken from Widrow & Dubinski (2005). The initial conditions assume $G = 1$, with units of kpc, 100 km s^{-1}, and 2.33×10^9 M$_\odot$.

Model	$\epsilon_{\rm h}$	$\sigma_{\rm h}$	$a_{\rm h}$	$M_{\rm d}$	$R_{\rm d}$	$h_{\rm d}$	$\epsilon_{\rm b}$	$\sigma_{\rm b}$	$a_{\rm b}$	Q
M1, D1	0.11	3.447	8.818	14.47	2.817	0.439	0.209	4.357	0.884	2.2
M2, D2	0.17	2.496	12.96	19.66	2.806	0.409	0.213	4.444	0.788	1.3

Table 2. Particle number and mass resolution of the components of the various models described in Section 2.

Model	Component	$N_{\rm p}$	$M_{\rm p}$ (M$_\odot$)
M1, D1	Disc	219 607 640	160
M1, D1	Bulge	21 960 680	540
M1, D1	Halo	878 431 120	640
M1	Dwarf stellar	153 599	4236
M1	Dwarf dark	2880 684	19 960
M1	Total	1123 033 723	–
M1, D1	Total host	1119 999 440	–
M2, D2	Disc	250 980 160	185
M2, D2	Bulge	25 097 920	482
M2, D2	Halo	1003 921 280	674
M2	Dwarf stellar	153 599	4236
M2	Dwarf dark	2880 684	19 960
M2	Total	1283 187 242	–
M2, D2	Total Host	1280 152 959	–

While we do not wish to perform a detailed re-analysis of existing models from the literature, Fig. 1 shows the rotation curve (left-hand column), along with the frequencies (middle column) and periods (right-hand column) in the radial (blue), vertical (grey), and azimuthal (orange) directions, for the initial discs (dotted lines) and the final state of the isolated discs (dashed lines) for Models D1 (top row) and D2 (bottom row).

The top row shows that Model D1, the high stability disc, experiences almost no change in rotation curve, frequency, or period over the course of the ∼5 Gyr of isolated evolution, in such that the dashed lines consistently almost cover the dotted lines. Similarly, the top row of Fig. 2 shows that Model D1 remains a smooth disc for several Gyr of evolution, with some very light spiral structure by the final snapshot at $t = 5.28$ Gyr. As such, there is no defined ‘present-day’ snapshot as the disc is never a good representation of the morphology of the MW. It is included in the paper and hosted on Flathub as Model D1, snapshot 200, purely to facilitate comparison with the M1 merger model presented later for which it is used as the host galaxy. We use the snapshot at ∼2 Gyr, which is ample time for the minor instabilities to have mixed away, and before the emergence of the mild spiral structure later on.

However, the lower row of Fig. 1 shows that Model D2 experiences significant evolution in its rotation curve, orbital frequencies, and periods as an isolated galaxy. Morphologically, the lower row of Fig. 2 shows that the initial condition develops into a barred galaxy with some weak spiral structure. We rotate the bar angle to approximately match the estimates of the MW bar angle with respect to the Solar position, assumed here to be $(x_\odot, y_\odot) = (-8.178, 0)$ kpc. At the final step at $t = 5.375$ Gyr, the pattern speed is $\Omega_{\rm b} = 26.7$ km s^{-1} kpc^{-1}, which is significantly slower than current estimates of the MW's bar pattern speed which appear to be converging around 37–42 km s^{-1} kpc^{-1} (e.g. Bovy et al. 2019; Clarke et al. 2019; Sanders, Smith & Evans 2019). Thus, the bar does not well match our current view of the MW bar, but again, that is not the purpose of this work, and we host the final snapshot[3] only for comparison with the merger model described below.

2.2 Dwarf galaxy properties

For simplicity, we use the initial condition for the Sagittarius-like dwarf galaxy from model L2 of Laporte et al. (2018b), henceforth called ‘the dwarf’, which is comprised of two Hernquist spheres (Hernquist 1990). The first represents the dark matter, and has virial mass $M_{200} = 6 \times 10^{10}$ M$_\odot$, concentration parameter $c_{200} = 28$, halo mass $M_{\rm h} = 8 \times 10^{10}$ M$_\odot$, and scale radius $a_{\rm h} = 8$ kpc. The second represents the stellar component embedded in the dark halo, where the stellar mass $M_* = 6.4 \times 10^8$ M$_\odot$ and $a_{\rm h} = 0.85$ kpc (see Laporte et al. 2018b, for a more thorough description).

2.3 Merger simulations, Models M1 and M2

Model M1 is the merger of the dwarf into the D1 Milky Way model. Model M2 is the merger of the dwarf into the D2 Milky Way model.

The top left panel of Fig. 3 shows the orbit of the dwarf in R, x, and z in Model M1 (referring to the combined system of D1 and the dwarf), with the horizontal dotted line marking the $R, x, z = 0$ line. The centre left panel of Fig. 3 shows v_x and v_z for the dwarf. Note that y and v_y are not shown as the merger is almost radial along the y-axis. The lower left panel shows the stellar (grey), dark (blue), and total (orange) mass within 5 kpc of the centre of the dwarf over the course of the simulation. The dwarf loses mass over time, with the ‘step’-like structure corresponding to the pericentric passages, as expected.

The right-hand column of Fig. 3 shows the same but for Model M2. The dwarf in Model M2 initially loses mass at a slower rate than M1, but becomes fully disrupted around 6.75 Gyr following rapid mass-loss in the fourth and fifth pericentric passages (note that the mass does not go to zero at $t > 6.75$ as the mass within 5 kpc of the median position of dwarf stars is still substantial in the inner galaxy; this is a simple spatial selection to illustrate mass-loss, not a rigorous census of bound stars).

We assess the orbital trajectories of the dwarf in Models M1 and M2, and define the ‘present-day’ snapshots as the times when the dwarf is closest to the location and motion of Sgr in the MW as given by Vasiliev & Belokurov (2020). For Model M1, we identify the most ‘present-day’-like snapshot as occurring at $t = 6.87$ Gyr, and for Model M2 we identify the most ‘present-day’-like snapshot as occurring at $t = 5.44$ Gyr. The ‘present day’ for both models is marked in Fig. 3 with a vertical dashed line.

Table 3 gives the position and motion of Sgr (Vasiliev & Belokurov 2020) and the dwarf in Models M1 and M2. For both models, as in the real MW–Sgr system, the dwarf is approaching a disc crossing, approximately 6 kpc beneath the disc plane, and on the far side of the galaxy from the Sun [considered to be at $(x_\odot, y_\odot) = (-8.178,$

---

[3] Model D2, snapshot 549 on Flathub.

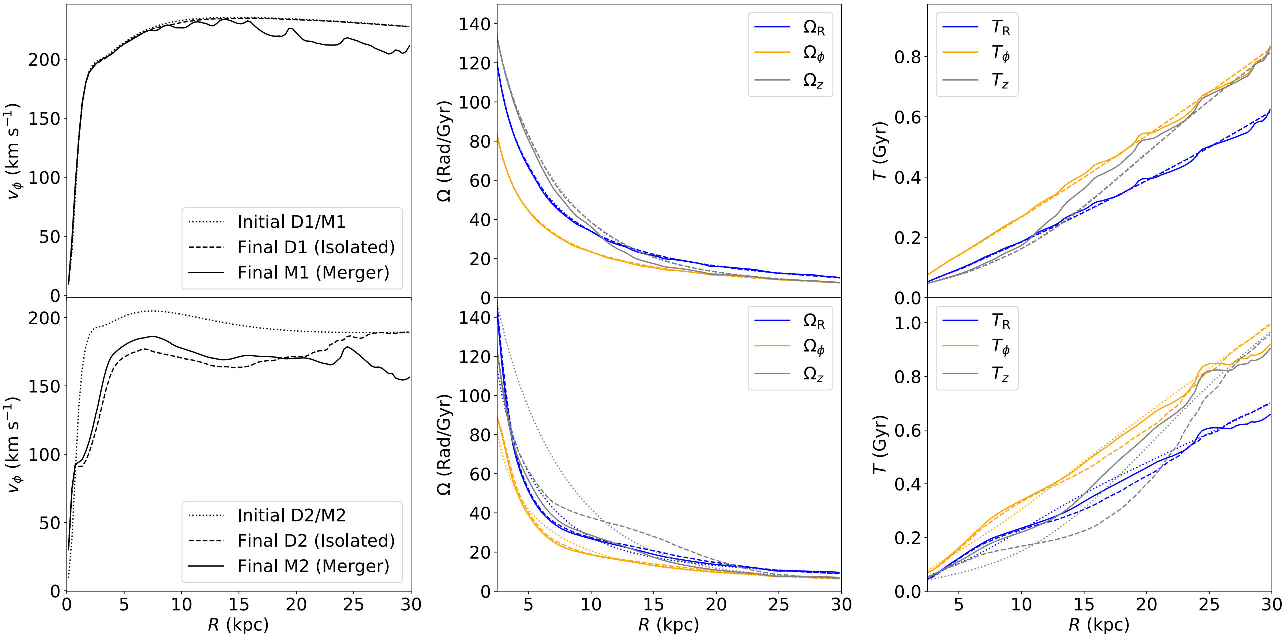

Figure 1. Rotation curve (left-hand column), orbital frequencies (centre column), and orbital period (right-hand column) for Model D1 and M1 (upper row) and Model D2 and M2 (lower row). The dotted lines show the initial condition, the dashed lines show the 'present-day' snapshots of the isolated discs D1 and D2, and the solid lines show the 'present-day' snapshots of Models M1 and M2. In the centre and right-hand columns, the radial, azimuthal, and vertical frequencies and periods are blue, orange, and grey, respectively.

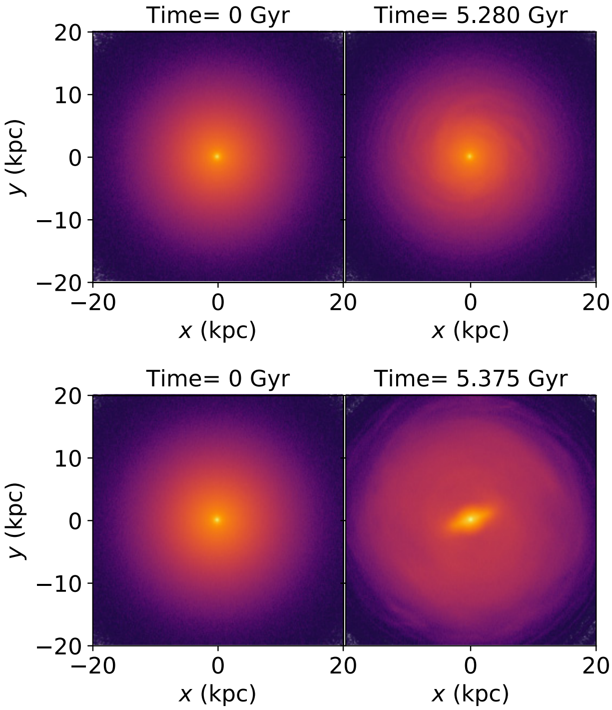

Figure 2. Face-on view of the isolated disc Models D1 (upper row) and D2 (lower row) at $t = 0$ (left-hand column) and at the end of the simulation (right-hand column).

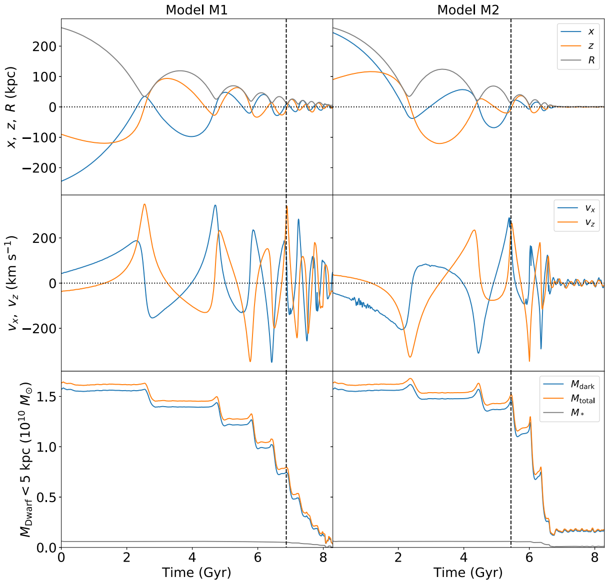

Figure 3. Orbital trajectory in spherical radius R (grey), x (blue), and z (orange, upper row) and velocity v_x (blue) and v_z (orange, middle row), and mass within 5 kpc for the dwarf in $10^{10}\,\mathrm{M}_\odot$, for stellar (grey), dark (blue), and total mass (orange, lower row) for Model M1 (left-hand column) and M2 (right-hand column). Note that y and v_y are not shown as the orbit is almost radial in the x–z plane. In Model M2, the satellite is fully disrupted around 6.75 Gyr. The vertical line shows the time chosen for the present day.

0) kpc], moving away from us roughly along the x-axis. However, in both models, our present-day snapshots have the dwarf too close to the galactic centre ($R = 11.6$ and 13.8 kpc, compared to $R_{\rm Sgr} = 18.8$ kpc). This is because at no point during the simulation are the dwarfs at the correct radius *and* the correct orbital phase. For example, we prioritized the phase of the orbit over the distance from the galactic centre.

In addition, at these 'present-day' snapshots the dwarf is significantly more massive than the remnant mass of $M_{\rm Sgr} \sim 4 \times 10^8\,\mathrm{M}_\odot$ inferred from the central velocity distribution (Vasiliev & Belokurov

Table 3. Sagittarius position and motion from the literature, and the location of the dwarfs at the 'present-day' model snapshots.

Model/catalogue	x (kpc)	y (kpc)	z (kpc)	v_x (km s^{-1})	v_y (km s^{-1})	v_z (km s^{-1})
Vasiliev & Belokurov (2020)	17.5	−2.5	−6.5	237.9	24.3	209.0
M1	9.5	−0.4	−6.7	115.7	5.9	311.9
M2	12.9	−0.5	−5.0	208.6	7.3	255.4

2020), and in each case the dwarf is significantly within the inner galaxy before the mass is comparable to that of the Sgr remnant. We are not concerned by the discrepancy as the purpose of these models is to investigate the response of the discs to the satellite perturber, and while such a response may be stronger in the simulation than the true MW, the dynamics should be qualitatively comparable. As such, we defer our attempt to better fit the MW–Sgr system to future work (Bennett, Bovy & Hunt 2021).

For the calculation of the orbits and the subsequent analysis of the dynamics in later sections, we re-centre the simulations on the centre of the bulge at each time-step as the host galaxies experience reflex motion owing to the in-falling satellites. We also realign the z-axis with the galaxy's axis of rotation, which can change over the course of the interaction, especially in the more violent merger of Model M2.

In summary, Model M1 is designed to be a laboratory for exploration of the formation and evolution of the $z-v_z$ phase spiral in an otherwise smooth disc. Model M2 is an example of a violent merger between a MW disc, and a large compact satellite. Future work will include construction of a closer representation of the MW–Sgr system (Bennett et al. 2021) but that is not the focus of this work, which investigates generic merger signatures.

3 MODEL M1 STRUCTURE AND KINEMATICS

Model M1 is designed to be a laboratory for exploration of the formation and evolution of disc substructure in an otherwise smooth disc.

3.1 Global snapshot of the 'present-day' state

Fig. 4 shows the stellar morphology and kinematics of Model M1 at the 'present day' of $t = 6.87$ Gyr.[4] The top left panel shows the face-on view of the surface density of the disc and dwarf, the top middle shows the mean radial velocity, the top right panel shows surface density in the edge-on view of the disc and dwarf, the lower right panel shows the morphology of the stellar component of the dwarf only. The lower left panel shows the mean vertical position, and the lower centre panel shows the mean vertical velocity. The dwarf particles are only shown in the edge-on views in the right-hand column, although its position is marked in the face-on views with a green dot. The downwards pull of the current passage of the dwarf is visible in the vertical velocity signature in the lower centre panel (see Gandhi et al. 2021, for a further discussion of this effect).

As one can see from the top left panel the 'present-day' snapshot of Model M1 contains no bar. It does develop one later in the simulation, and a slight hint of the emerging quadrupole can be seen in the inner region of the top centre panel, but it only becomes substantial once the dwarf is in the inner region of the galaxy (see here[5] for the full evolution of Model M1). Model M1 does contain numerous thin, low pitch angle spiral arms which are tidally induced by the interaction with the dwarf. Thus, Model M1 is an excellent laboratory to study the structural and kinematic features which arise from a satellite perturber, without contamination from bar resonances. However, it is not designed to be a 'best-fitting' model of the current state of the MW, and the lack of bar, high Q, and the location of the dwarf compared to the galactic centre mean that it should not be taken as such.

The solid lines in the top row of Fig. 1 show the rotation curve, orbital frequencies and periods for the 'present-day' snapshot. The rotation has fallen slightly in the outer galaxy, with the bumps corresponding to kinematic substructure induced by the satellite. The radial and azimuthal frequencies and periods do not change much in the highly stable disc, but the vertical frequencies (periods) drop (rise) as the disc is heated by the merging satellite.

3.2 Model M1: the phase spiral locally

As first highlighted by Antoja et al. (2018) with *Gaia* DR2, the vertical perturbation of the Galactic disc manifests as a spiral or snail shape in the $z-v_z$ plane. Dynamically, this can be attributed to the influence of an external perturber, or the buckling of the Galactic bar.

As shown in Li (2021) and Gandhi et al. (2021), the local phase snail as selected in spatial coordinates is a composite of phase snails with different angular momentum, J_ϕ. The upper left panel of Fig. 5 shows the local phase spiral as defined as all stars within 1 kpc from the 'Solar position' defined as $(x, y, z) = (-\ 8.178, 0, 0)$ in Model M1, where the v_z and z axes have been re-scaled by the vertical velocity dispersion σ_{v_z} and the vertical dispersion σ_z of the sample, respectively. For visualization purposes the distribution is smoothed with a Gaussian with a scale of 0.2 in the re-scaled coordinates, and we have subtracted the smoothed background distribution, such that the colourbar shows the difference in density between the data and the smoothed version, $\Delta\rho$. The smoothing, scaling, and colour bar are kept consistent across all subsequent phase spiral plots. The upper middle and right-hand panels show the $z-v_z$ spiral for selections within 3 and 5 kpc of the 'Solar position' merely to illustrate the importance of being able to resolve the spiral locally. Selecting a larger region distorts the morphology, as expected.

The middle row shows the split of stars from the $d < 1$ kpc sample into different angular momentum bins. The morphology of the lower row evolves with J_ϕ as shown in Li (2021) and Gandhi et al. (2021), because the phase spiral for stars selected purely in position space is an amalgamation of phase spirals from stars with different actions and different orbital histories which were located in different regions of the galaxy during the satellite perturbation (see Gandhi et al. 2021, for an illustration).

---

[4] Model M1, snapshot 703 on Flathub.

[5] https://users.flatironinstitute.org/~jhunt/M1-Morphology + Kinematics.mp4 (or.gif if mp4 is unsupported).

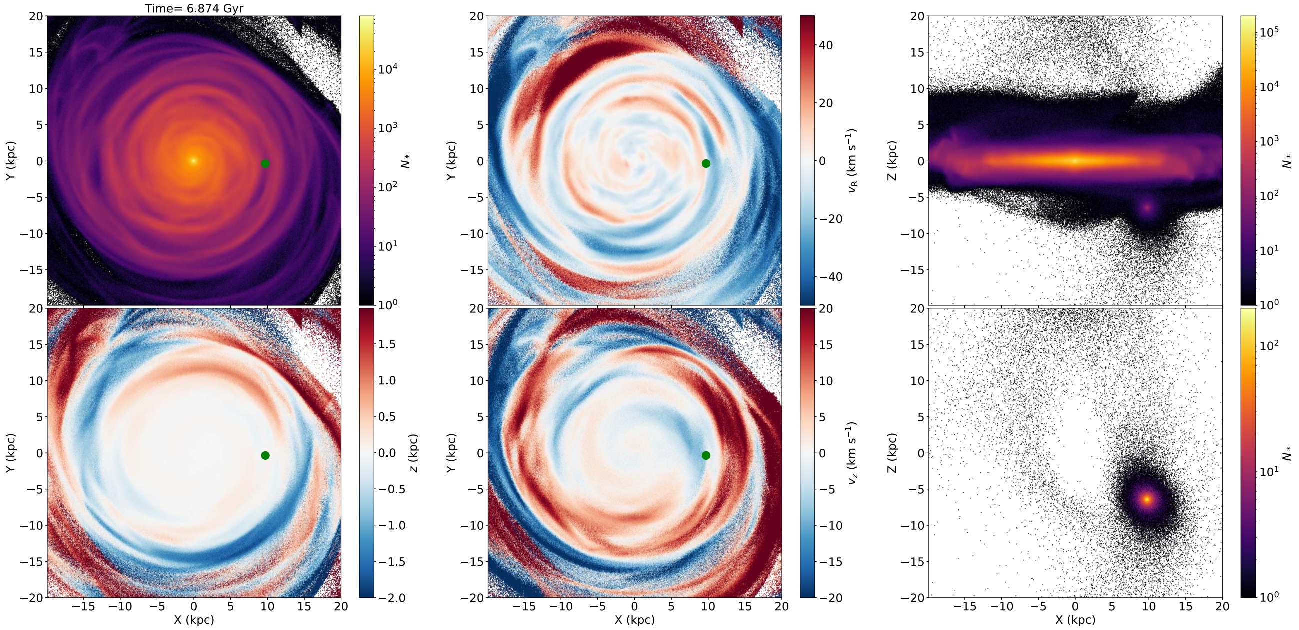

Figure 4. Face-on (left-hand and centre columns) and edge-on (right-hand column) view of the disc coloured by number count (upper left panel and right-hand column), mean radial velocity (upper centre), mean vertical position (lower left), and mean vertical velocity (lower centre) for Model M1 at $t = 6.874$ Gyr. The dwarf particles are only included in the right-hand column, but its position is marked with a green dot in the face-on panels.

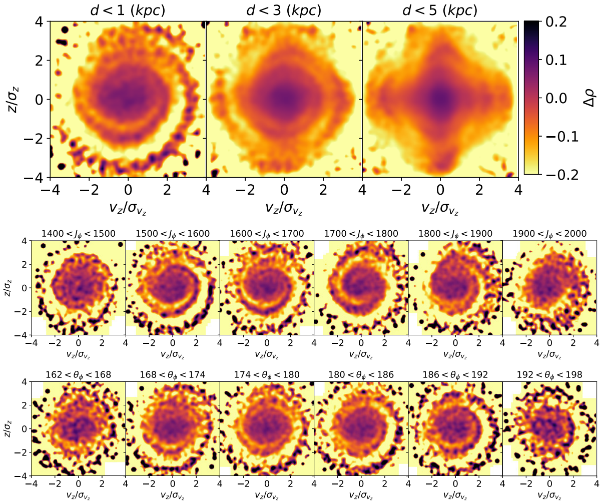

Figure 5. z–v_z spiral for particles within 1 kpc of the 'Solar location' at $(x, y, z) = (-8.178, 0, 0)$ kpc (upper left), within 3 kpc (upper middle) and within 5 kpc (upper right) in Model M1 at $t = 6.874$ Gyr. The middle and lower rows are the upper left ($d < 1$ kpc) selection of stars further subdivided into J_ϕ (middle row) and θ_ϕ bins (lower row).

Furthermore, as shown in our previous work Hunt et al. (2020), such a separation into different angular momentum bins, while retaining the physical azimuthal constraint is only half of the transformation from physical space into orbit space. Further refinement of the spiral should be possible by also selecting stars by their azimuthal phase angle, θ_ϕ, instead of their physical angle ϕ, although this intrinsically assumes a form for the Galactic potential. θ_ϕ is the angle of a star's guiding centre (e.g. see fig. 1 of Hunt et al. 2020) which increases linearly as it orbits the galaxy.

As such, the lower row of Fig. 5 shows the local phase spiral from the top panel split into θ_ϕ bins (where $\theta_\phi = 180$ deg is the Solar azimuth, and $\theta_\phi = 0$ is the far side of the galaxy). As with the selection in J_ϕ, the spiral evolves with θ_ϕ for stars within the 'local' volume. Similar to how stars with different actions are affected differently, so are stars with different azimuthal phase angles, because their initial position and motion with relation to the perturber will be different. This is to be expected, but has not been shown before to our knowledge.

Fig. 6 shows the phase spirals for the sample split by J_ϕ (displayed as $R_{\rm G}$) along the x-axis and by θ_ϕ along the y-axis. Note that a 1 kpc volume around the Sun covers ~7 deg in galactic azimuth, ϕ, yet this expands to nearly 60 deg in phase in the associated angle, θ_ϕ, while still resolving the phase spirals for around 30 deg. Similarly, 1 kpc in galactocentric radius, R, contains stars for several kpc in $R_{\rm G}$ and lets us track the phase spiral for around 3 kpc radially. The morphology clearly evolves along both axes, and higher resolution models may be able to track the phase spiral even further from a local volume. Stars with the same J_ϕ but different θ_ϕ show different morphology in the phase spiral, as do stars with the same θ_ϕ but different J_ϕ, as expected.

This splitting of phase spirals by stars with shared orbital histories further illustrates the variety of morphologies contained within the 'Solar neighbourhood' phase spiral, and the significant amount of information which is lost when considering only the present-day position of the stars and not their orbital histories. Analysing the phase spiral as a function of action-angle coordinates will enable us to probe the strength and time-scale of a past impact at a range of positions around the galaxy, and may help us to constrain both the properties of the perturber, and the galactic potential, but we defer this to future work.

3.3 Model M1: the phase spiral globally

A lot of attention has been paid to the local z–v_z spiral since its discovery by Antoja et al. (2018), but there also exists a spiral pattern in vertical position and motion which arises across the disc plane

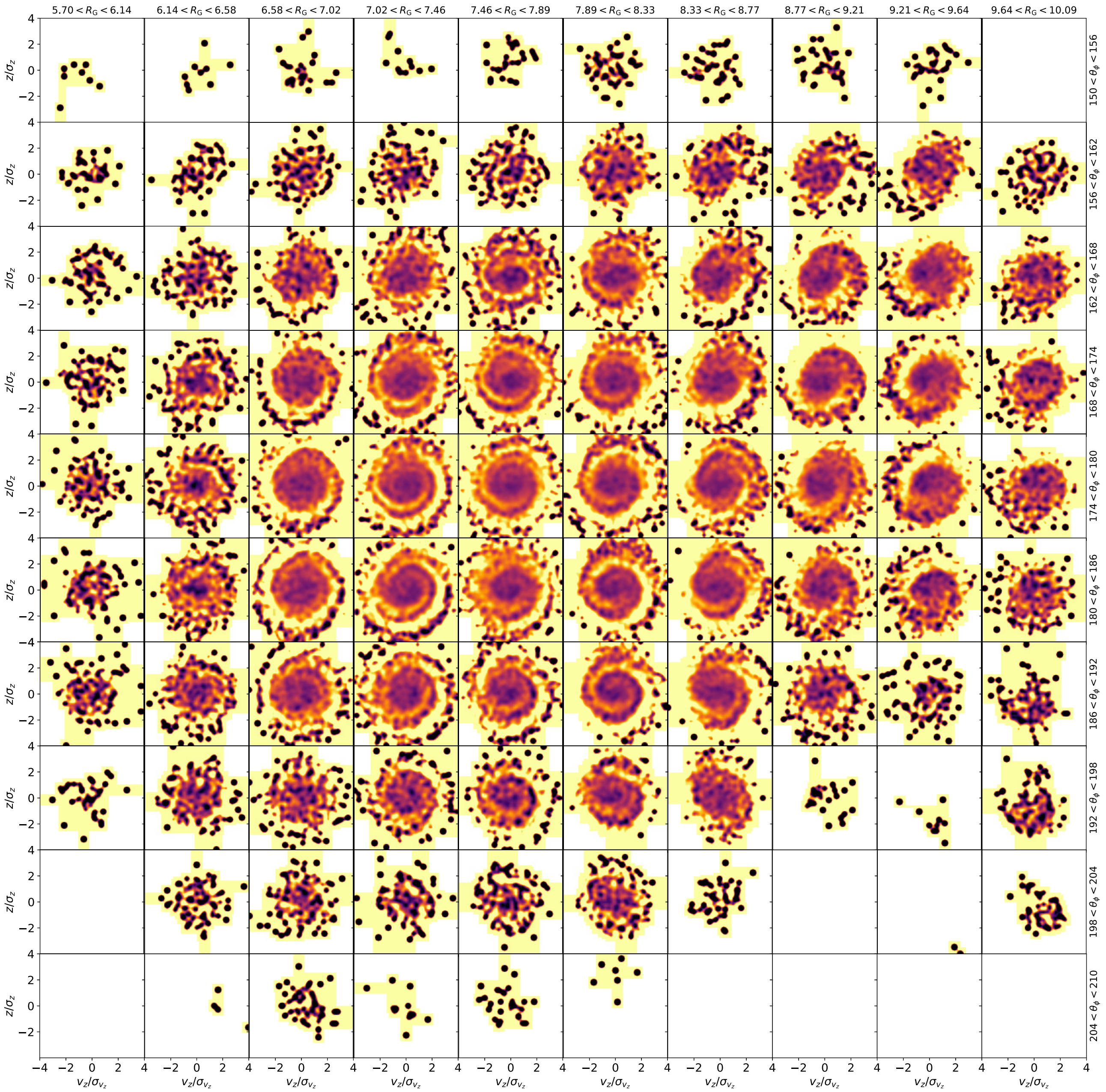

Figure 6. $z-v_z$ plane for a sample of stars within a 1 kpc box selection around the Solar neighbourhood, split by J_ϕ (km s^{-1} kpc, different columns) and θ_ϕ (deg, different rows).

(e.g. Gómez et al. 2013; Laporte et al. 2019; Gandhi et al. 2021). It is difficult to resolve this global kinematic spiral in the actual MW data, as we struggle to track the kinematics far from the Solar neighbourhood (although see Eilers et al. 2020), but there is no reason we cannot examine it further in the simulations, and it is of course merely a different projection of the same vertical motion, and the same vertical asymmetry.

As a reminder, in Fig. 4 the face-on panels coloured by mean z (lower left) and mean v_z (lower middle) show that the mean vertical position and motion of stars also exhibits spiral structure when viewed across the plane. These are a local collapsing of the phase spirals into their offset (or asymmetry) in either vertical position or velocity, albeit at a finer resolution than allowed when binning to resolve the phase spiral. However, with high-resolution disc models we can resolve well-defined phase spirals on the kpc scale all across the disc.

As shown in Section 3.2, it is useful to select the phase spirals as a function of J_ϕ and θ_ϕ. Thus, following Hunt et al. (2020), we transform the physical coordinates (x, y) into guiding centre Cartesian coordinates $(x_{\rm act}, y_{\rm act}) = (J_\phi/v_{\rm circ}\cos\theta_\phi, J_\phi/v_{\rm circ}\sin\theta_\phi)$, in order to group stars by their shared orbital history instead of their current physical location. Such a selection is not possible in the *Gaia* data owing to selection effects, but it is straightforward in the simulation (see Hunt et al. 2020, for a more thorough description of this transformation and its limitations).

Fig. 7 shows the face-on view of Model M1, in guiding centre Cartesian coordinates, divided into 1 kpc × 1 kpc bins, where each bin displays the phase spiral for the star particles contained within

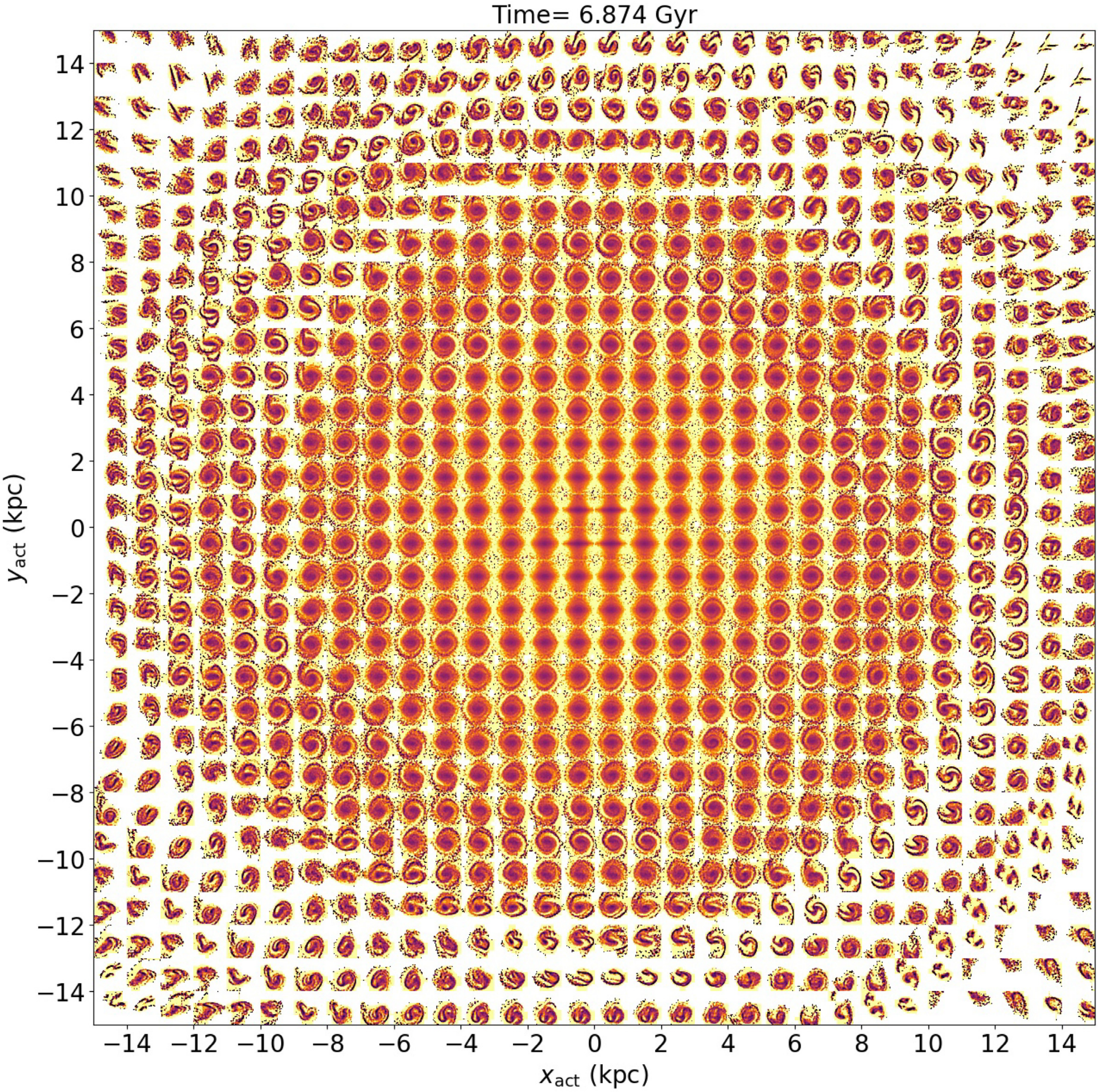

Figure 7. The phase spirals shown across the face of Model M1 at $t = 6.874$ Gyr, in 1 × 1 kpc bins from X, $Y = -15$ to 15 kpc. Note that the global vertical spiral is visible owing to the offset of the individual phase spirals from $(v_z, z) = (0, 0)$ and the v_z axes have been re-scaled to compensate for the change in velocity dispersion with radius (see the text). For the animated version of the evolution over time see https://users.flatironinstitute.org/~jhunt/M1-AASpiral.mp4 (or.gif if mp4 is unsupported).

(see Fig. 5 for the axis scale and colour bar for each individual spiral). First, note that the $z-v_z$ phase spirals occur globally, not in an isolated region of the disc, but also note that their morphology and offset from the centre of each bin differs with location across the galaxy. This change in offset/asymmetry causes the larger spiral visible across the disc, as is shown in the vertical position and motion in Fig. 4.

Fig. 8 shows the face-on view of the 'present-day' snapshot of Model M1, coloured by $\bar{A}_z$, a simple model of the vertical epicyclic amplitude given by $A_z = (v_z/\Omega_z + z^2)^{1/2}$. The colourbar is such that the stars with the highest deviation from planar position or motion are in white, matching the offset of stars from the centre of the individual bins in Fig. 7, which traces out the global vertical spiral. The relation between the plane of phase spirals in the upper panel and the mean vertical epicyclic amplitude, which encompasses the offset in both axes is clear.

A significant amount of information is also contained within the time evolution of both the global and local vertical spirals. The time evolution of Fig. 7 is available online.[6] We encourage the reader to make use of the animation to visualize the propagation of the

---

[6] https://users.flatironinstitute.org/~jhunt/M1-AASpiral.mp4 (or.gif if mp4 is unsupported).

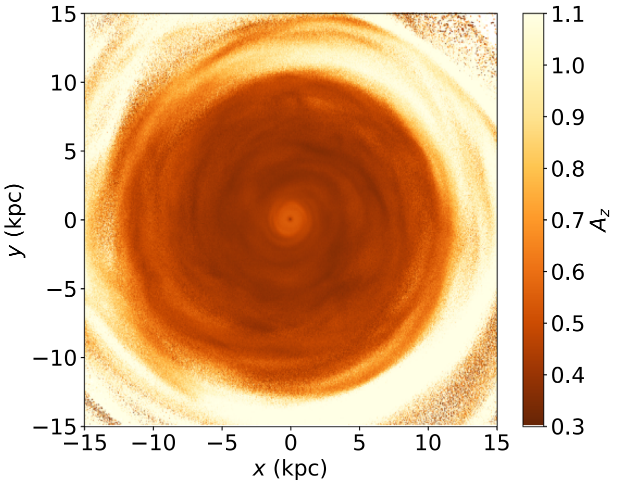

Figure 8. Face-on map of vertical epicyclic amplitude, $A_z = (v_z/\Omega_z + z^2)^{1/2}$ for Model M1 present-day snapshot, $t = 6.874$ Gyr.

response to the repeated passages of the dwarf across the disc and the formation and evolution of the $v-v_z$ phase spirals.

While the $z-v_z$ spirals close to the Solar circle are relatively well behaved in Fig. 7, those in the outer galaxy are more chaotic, being comprised of a mix of phase spirals induced by multiple passages (see also Laporte et al. 2019). The animated version of Fig. 7[6] shows that the first passage of the dwarf at $t = 2.54$ Gyr causes only a small ripple across the global plane, but it is enough to perturb the disc from vertical equilibrium and seed the creation of the phase spirals, which propagate through the outer disc for over 2 Gyr before the second pericentric passage occurs at $t = 4.74$ Gyr (see Fig. 3 for the orbit). Fig. 9 shows as Fig. 7, but at $t = 4.74$ Gyr, which is 2.2 Gyr after the first pericentric passage of the dwarf. The $z-v_z$ phase spirals around $R_{\rm G} = 15$ kpc are well defined within the 1 kpc boxes following the single passage, highlighting the benefit of the increased phase space resolution of the disc.

3.3.1 *Bending and breathing behaviours, and the resulting phase spirals*

Interestingly, following the first passage, the phase spirals are two armed, as opposed to the single arms visible at later times (e.g. Figs 5–7, or the later stages of the animation). We argue that this is to be expected owing to the changing nature of the interaction between the disc stars and the dwarf over the course of the merger (see also Poggio et al. 2021; Grion Filho et al. 2021 for an exploration of the changing nature of the interaction between the dwarf and satellite on a global scale in the L2 model of Laporte et al. 2018b).

The first passage occurs at a large radius (∼35 kpc), with high vertical velocity (∼350 km s^{-1}), which is a rapid, almost entirely perpendicular passage through the outer part of the galaxy, where the satellite velocity is much greater than the maximum vertical velocity of the stars (∼80 km s^{-1} at ≥15 kpc). The interaction time-scale is of the order of $h_{\rm d}/v_{z,{\rm sat}} = 0.439\,{\rm kpc}/350\,{\rm km\,s}^{-1} \approx 1.2$ Myr, which is significantly faster than the vertical period of the orbits (see Fig. 1).

The rapid transit also leaves little time for the stars to travel azimuthally, meaning that overall they receive an approximately equal force upwards and downwards. As previously shown in Widrow et al. (2014), such an interaction excites a breathing motion in the disc, owing to the short time-scale of the interaction, and the high relative velocity between the perturber and the disc stars.

Conversely, the later passages have increasingly longer interaction times and a smaller difference in vertical velocity. For example, the second and third disc crossings are close together in time ($t = 4.40$ and $t = 4.85$, with the pericentre in between). The interaction time-scales here are of the order of $R_{\rm cross}/v_{z,{\rm sat}} = 74\,{\rm kpc}/130\,{\rm km\,s}^{-1} \approx 557$ Myr and $R_{\rm cross}/v_{z,{\rm sat}} = 38\,{\rm kpc}/230\,{\rm km\,s}^{-1} \approx 162$ Myr for the second and third disc crossings, respectively, and the orbital path is such that the dwarf exerts a continuous influence on the disc while passing below the galaxy and remaining comparatively close to the disc plane for an extended period of time (see Fig. 3). Such interactions on the hundreds of Myr scale are then comparable to the disc frequencies (see Fig. 1), and should induce bending waves (which would be strongest when the satellite is in resonance with the disc stars; Sellwood, Nelson & Tremaine 1998).

The behaviour of the stars themselves is also dependent on the vertical phase angle of their orbit, θ_z. In brief, in a high-velocity, rapid interaction, stars with $\theta_z = 0$ or π (apocentres) both gain energy, while stars with $\theta_z = \pm\pi/2$ (pericentres) will lose energy, stretching the $z-v_z$ phase space distribution and creating a breathing motion. Conversely, in a slower interaction, for two stars spaced by π in angle, one will gain energy and one will lose energy, resulting in an overall shift in the distribution and the creation of a bending motion (see section 2 of Widrow et al. 2014, for a thorough explanation and illustration).

To our knowledge this has not been shown in other MW–Sgr merger studies, which have typically focused on the latter stages of the merger (although see Laporte et al. 2018b), by which point the interaction is on the time-scale and relative velocity to create bending modes (e.g. Bland-Hawthorn & Tepper-García 2021) and thus the one armed spirals. Thus, it is possible that relics of such two armed 'breathing spirals' could exist in the outer disc of the MW (e.g. as seen at around $R_{\rm G} = 13$ kpc in Fig. 7), and they could be resolvable with future surveys. While the orbital trajectory of Sgr is not well known over time-scales of several Gyr it is likely that early interactions were relatively quick, and the disc should contain both bending and breathing motions (e.g. Widrow et al. 2014). As shown in Laporte et al. (2019), while subsequent passages of a satellite can erase the signatures of previous perturbations in the Solar neighbourhood, the longer orbital time-scales in the outer disc make it more likely that multiple patterns can coexist. Regardless, we consider this an example of an interesting dynamical phenomenon brought to light by the high phase space resolution in the outer disc.

3.4 Model M1: planar dynamics and the classical moving groups

While most of the recent interest in the impact of Sgr upon the disc of the MW has been regarding the vertical kinematics, it has also been shown that such mergers reproduce similar ridge structure as are present in the $R-v_\phi$ plane (Laporte et al. 2019) and arches in the $v_{\rm R}-v_\phi$ plane (Khanna et al. 2019) which were previously predicted in Minchev et al. (2009). Fig. 10 shows the $R-v_\phi$ plane for the 'present-day' snapshot of Model M1 for star particles with $-\pi/32 < \phi < \pi/32$, coloured by number density (top panel), radial velocity (second panel), vertical velocity (third panel), and vertical position (bottom panel). As with previous studies, it is unsurprising to find significant structure in this space, despite the lack of a galactic bar, which is often invoked to create such features through resonant interaction with the disc (e.g. Fragkoudi et al. 2019; Asano et al. 2020). The magnitude of the radial velocity and vertical velocity

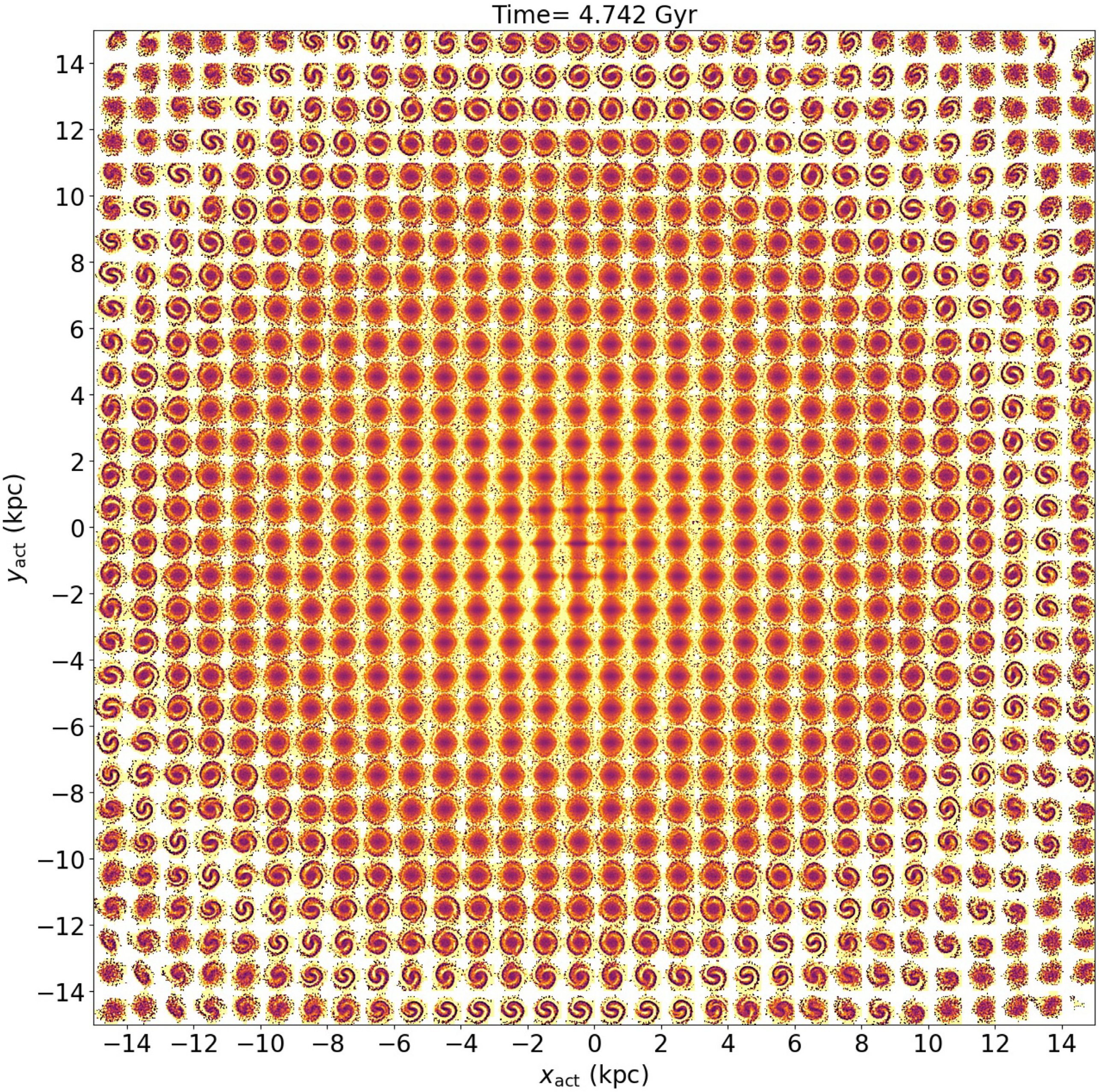

Figure 9. As Fig. 7, but for $t = 4.73$ Gyr, the time of the second pericentric passage. The phase spirals currently present were excited by the first pericentric passage, 2.19 Gyr in the past.

pattern are both approximately double that observed in the *Gaia* data, but this is to be expected owing to the high mass of the dwarf remnant in Model M1.

The real advantage of having high phase space resolution in the disc is that we can resolve the $v_{\mathrm{R}}-v_{\phi}$ plane over a smaller local volume than previous studies (e.g. Khanna et al. 2019). While we still cannot match the resolution of the *Gaia* data, we can easily pick out several moving groups when selecting regions on the kpc or less scale at the Solar radius. For example, Fujii et al. (2019) have previously used `Bonsai` simulations to examine the $v_{\mathrm{R}}-v_{\phi}$ plane around the Outer Lindblad Resonance (OLR) of a short fast bar. Similar to previous studies (e.g. Dehnen 2000) they find it causes a Hercules-like stream, a well-known moving group in the Solar neighbourhood, but only in approximately 50 per cent of snapshots. At other times it is disrupted or concealed by interaction with galactic spiral structure.

However, as mentioned above, numerous recent measurements of the bar pattern speeds favour a slower bar of around 40 km s^{-1} kpc^{-1} (e.g. Portail et al. 2017; Bovy et al. 2019; Clarke et al. 2019; Sanders et al. 2019), which would put the OLR a few kpc outside the Solar neighbourhood, and no longer possible to cause the Hercules stream. Instead, a ‘slow’ bar with pattern speed around 40 km s^{-1} kpc^{-1} will influence the local kinematics in the region of Hercules, through either the corotation resonance (Pérez-Villegas et al. 2017), or the 4:1 OLR (Hunt & Bovy 2018). However, the corotation resonance of a reasonable strength bar generally produces a significantly weaker Hercules-like stream than is seen in the data (e.g. Binney 2018; Hunt et al. 2018), although see also Monari et al. (2019), who use the

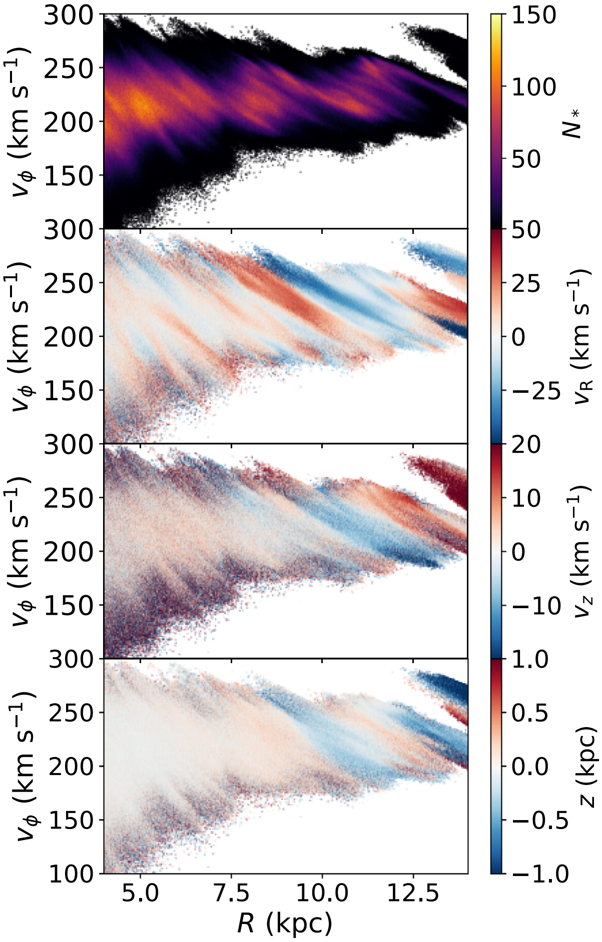

Figure 10. $R-v_\phi$ distribution coloured by number count (top panel), mean radial velocity (km s^{-1}, second panel), mean vertical velocity (km s^{-1}, third panel), and mean vertical position (kpc, bottom panel) for Model M1 at the 'present-day' snapshot.

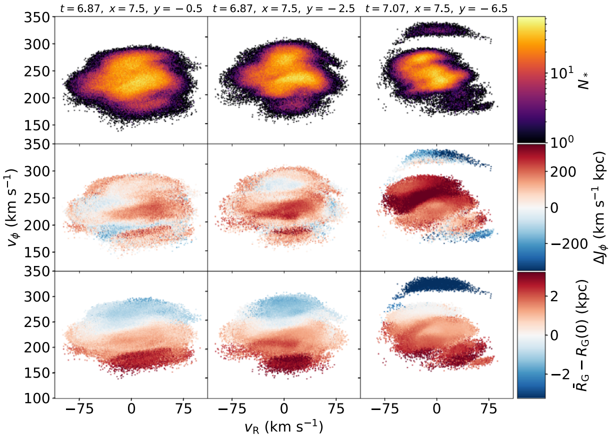

Figure 11. v_R-v_ϕ distribution coloured by number count (upper row), change in angular momentum, ΔJ_ϕ (km s^{-1} kpc) from the initial condition (middle row), and initial guiding radius with respect to the current location of the sample (lower row) for three local samples in the 'present-day' snapshot (left-hand and middle column) and 200 Myr later (right-hand column).

Portail et al. (2017) potential. Similarly, if Hercules is caused by the 4:1 OLR, then we would expect a strong OLR feature in a region of velocity space which is not observed in the Solar neighbourhood (for a thorough discussion of the kinematic signature of bars with fixed pattern speeds, see Hunt et al. 2019; Trick et al. 2021, and references within).

Alternatively, Chiba, Friske & Schönrich (2021) proposed the 'resonance sweeping' of a slowing bar as a mechanism for the creation of the Hercules stream and other Solar neighbourhood kinematics, an appealing explanation which can reconcile direct measurements of the Galactic bar's slow pattern speed with the strength of the kinematic substructure induced by the corotation resonance observed in the Solar neighbourhood. More recently, Chiba & Schönrich (2021) show that such a slowing bar creates a Hercules-like stream which is metal rich by 0.1–0.2 dex, owing to the constituent stars originating in the inner galaxy.

We do not intend or expect to match the Solar neighbourhood v_R-v_ϕ plane in Model M1, which is a model with no bar, and a disc with $Q=2.3$. However, similar to previous studies of the impact of spiral structure on the local velocity distribution (Hunt et al. 2018, 2019), we find it straightforward to locate regions with a Hercules-like feature in the appropriate part of velocity space in the model prior to bar formation. It is not straightforward to examine the metallicity of this region as Model M1 is a pure N-body simulation without gas or star formation. However, we can track the radial migration the star particles experience during the merger to see if our Hercules-like streams originate in the inner galaxy, which we would expect to be more metal rich.

The top row of Fig. 11 shows the v_R-v_ϕ planes for three regions close to the Solar radius in the present-day snapshot of Model M1 (left two columns) and one from 175 Myr afterward which bares a striking resemblance to the actual Solar neighbourhood v_R-v_ϕ plane (right-hand column). Each has a small separate moving group with low v_ϕ and positive v_R, qualitatively similar to the Hercules stream in the Solar neighbourhood. The second row shows the v_R-v_ϕ plane coloured as a function of the mean change in angular momentum, ΔJ_ϕ (km s^{-1} kpc), since the start of the simulation. The third row shows the difference between the initial guiding radius, $R_G(0)=J_\phi(0)/v_{\mathrm{circ}}$, which is a proxy for their birth radius, which is in turn a proxy for their metallicity, relative to the current guiding radius of the sample of the star particles.

In each case, we see that the Hercules-like moving group is mainly comprised of 'red' stars from the inner galaxy which have migrated outwards, with low initial $R_G(0)$, and positive migration, $\Delta J_\phi > 0$. Hence, the Hercules-like group in each case would be more metal rich. In addition, the largest implied metallicity occurs in the centre of the outwards moving group, similar to as found by Chiba & Schönrich (2021) for the slowing bar model, while we also see that the 'horn' feature present in the right-hand column is 'metal rich', as seen in the data, but not in the slowing bar model.

We are certainly not claiming that the MW does not contain a bar, or that it does not impact the kinematics of the disc stars. Both those statements are undoubtedly false, but as discussed before (Hunt et al. 2019) we remind the reader that it remains dangerous to make measurements of bar length, strength or pattern speed from a feature which can be explained by a different origin, or at the very least could be distorted by other non-axisymmetric structure.

In the case of the real data, the local v_R-v_ϕ distribution is likely to have been shaped by a combination of the Galactic bar, spiral structure and the perturbation of the disc caused by the interaction of the MW and its satellite galaxies, and disentangling them based on phase space information and metallicity alone is non-trivial. High-resolution simulations containing a MW-like galactic bar, spiral structure and satellite perturbers may help us break the degeneracy.

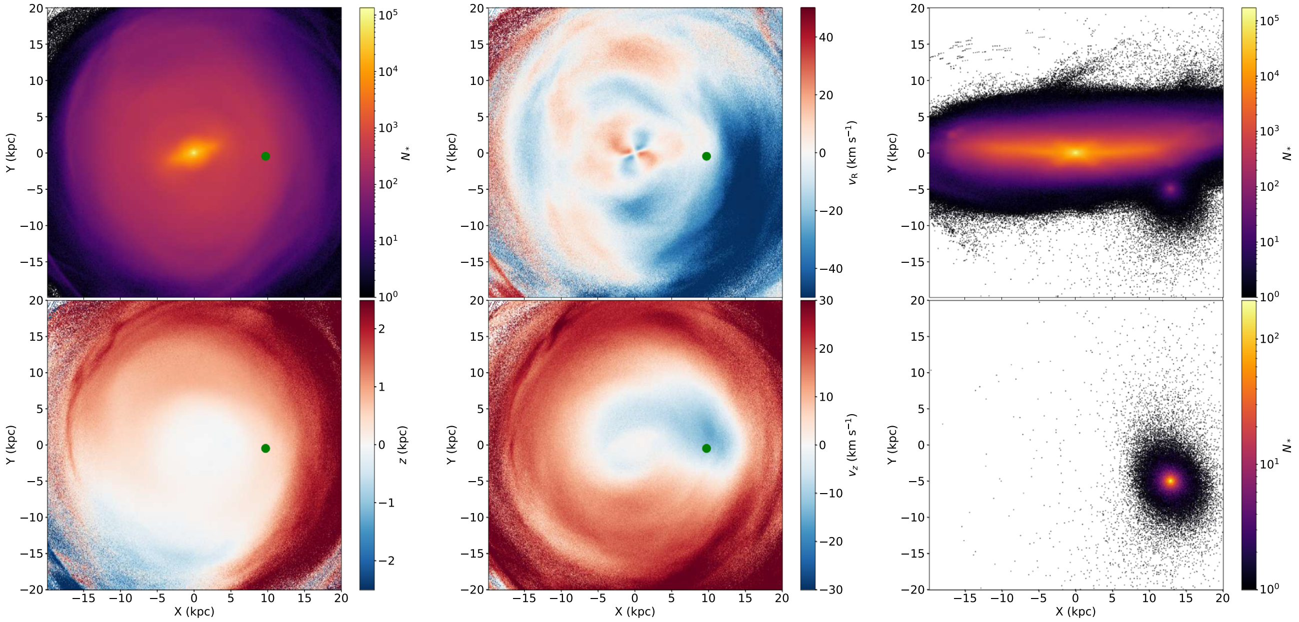

Figure 12. Face-on (left-hand and centre columns) and edge-on (right-hand column) view of the disc coloured by number count (upper left panel and right-hand column), mean radial velocity (upper centre), mean vertical position (lower left), and mean vertical velocity (lower centre) for Model M2 at $t = 5.44$ Gyr. The dwarf particles are only included in the right-hand column, but its position is marked with a green dot in the face-on panels.

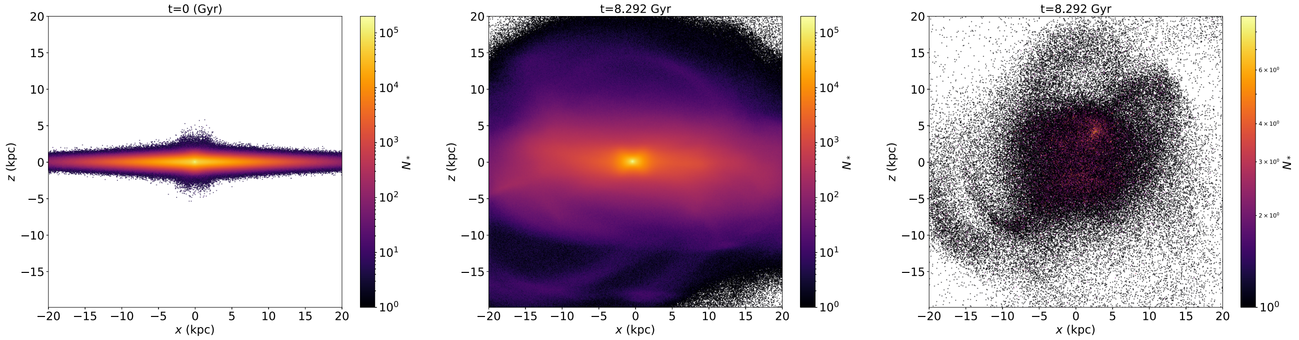

Figure 13. Edge-on view of Model M2 at $t = 0$ (left-hand panel) and $t = 8.292$ (Gyr, middle panel), and just the accreted stars from the dwarf at $t = 8.292$ (right-hand panel).

4 MODEL M2 STRUCTURE AND KINEMATICS

Fig. 12 shows the face- and edge-on morphology and kinematics for Model M2, as detailed above for Fig. 4. In this snapshot, the dwarf is a little closer to the true location of Sgr in the MW than Model M1. However, it is significantly less disrupted and has barely started to form a tidal stream making it a worse model of the overall system. In addition, as the dwarf remains significantly more concentrated, the force acting on the disc by the more massive remnant causes significant perturbation even at this early stage of the Merger, creating a strong warp. By the time the dwarf starts to disrupt it is further inside the Solar circle (see Fig. 3), and has caused significant perturbation to the disc beyond what is observed in the MW. For this reason, we do not consider the 'present-day' snapshot of Model M2 defined by the position of the dwarf to be appropriate for comparison with our own Galaxy in respect to the current interaction of the MW and Sgr. Instead, it is interesting as a high-resolution model of a more violent merger.

For example, Model M2 is potentially similar to violent merger events much earlier in the MW's accretion history. Such mergers have been proposed to be responsible for the creation of the MW's thick disc (e.g. Quinn, Hernquist & Fullagar 1993), although other explanations exist, such as the merger of numerous small satellites (e.g. Abadi et al. 2003), *in situ* formation following a gas-rich merger (e.g. Brook et al. 2004), the heating of the disc by radial migration (e.g. Schönrich & Binney 2009) or inheritance at birth through the properties of turbulent gas at high redshift (e.g. Noguchi 1998; Bournaud, Elmegreen & Martig 2009). Fig. 13 shows the edge-on view of Model M2 at $t = 0$ (left-hand panel), and $t = 8.29$ (Gyr, middle panel), and the accreted dwarf stars at $t = 8.29$ (right-hand panel).[7] The disc clearly experiences a significant thickening during the merger, and there remains numerous structures in the heated disc. The dwarf stars are well dispersed within ∼5 kpc, with some stream-like structure remaining in the outer galaxy. The lack of gas in Model M2 will prevent any subsequent formation of a replacement thin disc, but we can examine the thickened stellar disc and newly formed inner halo, and probe the dynamics of the accreted stars.

---

[7] Model M2, snapshot 557 on Flathub.

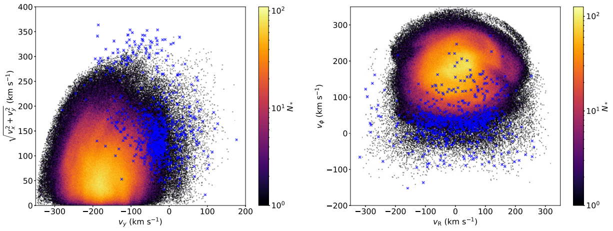

Figure 14. Toomre diagram (left) and the $v_\mathrm{R}-v_\phi$ plane (right) for the disc stars (histogram) overlayed with the accreted stars from the dwarf (blue crosses) both selected within 2 kpc of a Solar-like position of $(x, y, z) = (-8.178, 0, 0)$ kpc.

Fig. 14 shows the Toomre diagram (left; Sandage & Fouts 1987) and the $v_\mathrm{R}-v_\phi$ plane (right) for the disc stars (histogram) overlayed with the accreted stars from the dwarf (blue crosses) both selected within 2 kpc of a Solar-like position of $(x, y, z) = (-8.178, 0, 0)$ kpc. The left-hand panel shows the local accreted stars (blue crosses) on more radial orbits slightly outside the main disc volume (histogram). This is similar to fig. 1 of Helmi et al. (2018) comparing their merger simulation to the *Gaia*–Enceladus stars. Note that our merger is slightly prograde instead of slightly retrograde, as the model was not tailored to the *Gaia*–Enceladus merger event. Similarly, the right-hand panel shows the accreted stars on radial orbits reproduce the 'Sausage'-like structure as shown in Belokurov et al. (2018).

An *N*-body model of an isolated system is of course a less effective representation of the long-term evolution of a MW-like galaxy when compared to cosmological simulations that contain a full merger history while also encapsulating additional physics such as star formation and feedback. However, such simulations are, by necessity, lower resolution than isolated discs (although see Grand et al. 2021) and we make the final step of Model M2 available as an example of a high-resolution violent merger, which despite the lack of gas, none the less captures the satellite disruption and impact on the pre-existing disc.

5 CONCLUSIONS

In this work, we present two >1 billion particle self-consistent simulations of a dwarf galaxy merging into a MW-like disc galaxy, and the two isolated galaxies for comparison.

Model M1 is a merger into a highly stable disc (D1, $Q = 2.3$) where the non-axisymmetric structure all arises from the merger, making it a good laboratory to investigate the response. Model M2 is a more violent merger into a more massive disc (D2) which experiences significant disruption similar to mergers earlier in the MW's formation history, which produces a thick disc and an accreted population qualitatively similar to stars from the *Gaia*–Enceladus merger, both in the Toomre diagram and the 'Sausage' in the $v_\mathrm{R}-v_\phi$ plane. All are freely available on Flathub.[8]

Using Model M1, we illustrate the ability to resolve both vertical and planar kinematic substructure over a local volume, and show the emergence and evolution of the $z-v_z$ phase spirals globally across the disc. Our three main conclusions are as follows:

(i) We observe for the first time the different morphology of the $z-v_z$ phase spirals which arise from a breathing motion excited by an early rapid disc crossing (two armed spiral) compared to those which arise from bending modes (one armed spiral) during later slower disc crossings.

(ii) We show that these relics of earlier disc crossings are seen for multiple Gyr, especially in the outer galaxy, and shorter simulations of only the latter stages of such a merger may miss some complexity in both the resulting $z-v_z$ phase spirals and the global dynamics. Such relics could act as fossils into prior perturbations and/or laboratories to studying the growth rate of our own Galaxy (e.g. Laporte et al. 2020).

(iii) We show that Model M1 creates numerous Hercules-like moving groups in local planar kinematics, despite the lack of tailoring of the simulation to the MW or the presence of a Galactic bar. These moving groups originate in the inner galaxy, and would be metal rich compared to the rest of the $v_\mathrm{R}-v_\phi$ plane, as observed in the Solar neighbourhood data.

Finally, we remind the reader that while these models are an interesting high-resolution exploration of merger dynamics, they are not tailored to the MW–Sgr system, or the *Gaia*–Enceladus merger. For future work, we intend to create and release simulations of more MW-like systems, merging with more Sgr-like dwarf impactors (Bennett et al. 2021), and also include the Magellanic clouds, which are likely important for the present-day state of the overall system (e.g. Gómez et al. 2015; Laporte et al. 2018a; Garavito-Camargo et al. 2019; Cunningham et al. 2020; Vasiliev, Belokurov & Erkal 2021).

ACKNOWLEDGEMENTS

We thank the referee for a constructive report. JASH is supported by a Flatiron Research Fellowship at the Flatiron institute, which is supported by the Simons Foundation. KVJ was supported by National Science Foundation (NSF) grant AST-1715582. CFPL acknowledges funding from the European Research Council (ERC) under the European Union's Horizon 2020 research and innovation programme (grant agreement no. 852839). This work was supported in part by World Premier International Research Center Initiative (WPI Initiative), MEXT, Japan. This research made use of ASTROPY, a community-developed core PYTHON package for Astronomy (Astropy Collaboration 2013, 2018), and the galactic dynamics PYTHON packages GALPY (Bovy 2015), AGAMA (Vasiliev 2019), and GALA (Price-Whelan 2017). This work was performed in part at Aspen Center for Physics, which is supported by National Science Foundation grant PHY-1607611. This work was partially supported by a grant from the Simons Foundation.

DATA AVAILABILITY

The simulations are available on Flathub, at https://flathub.flatironinstitute.org/jhunt2021.

REFERENCES

Abadi M. G., Navarro J. F., Steinmetz M., Eke V. R., 2003, ApJ, 597, 21
Antoja T. et al., 2018, Nature, 561, 360
Asano T., Fujii M. S., Baba J., Bédorf J., Sellentin E., Portegies Zwart S., 2020, MNRAS, 499, 2416
Astropy Collaboration, 2013, A&A, 558, A33
Astropy Collaboration, 2018, AJ, 156, 123
Bédorf J., Gaburov E., Portegies Zwart S., 2012, J. Comput. Phys., 231, 2825
Bédorf J., Gaburov E., Fujii M. S., Nitadori K., Ishiyama T., Portegies Zwart S., 2014, Proceedings of the International Conference for High Performance Computing. p. IEEE, 54

---

[8] https://flathub.flatironinstitute.org/jhunt2021

Belokurov V., Erkal D., Evans N. W., Koposov S. E., Deason A. J., 2018, MNRAS, 478, 611
Bennett M., Bovy J., 2021, MNRAS, 503, 376
Bennett M., Bovy J., Hunt J. A. S., 2021, preprint (arXiv:2107.08055)
Binney J., 2018, MNRAS, 474, 2706
Binney J., Schönrich R., 2018, MNRAS, 481, 1501
Bland-Hawthorn J., Tepper-García T., 2021, MNRAS, 504, 3168
Blitz L., Spergel D. N., 1991, ApJ, 379, 631
Bournaud F., Elmegreen B. G., Martig M., 2009, ApJ, 707, L1
Bovy J., 2015, ApJS, 216, 29
Bovy J., Leung H. W., Hunt J. A. S., Mackereth J. T., García-Hernández D. A., Roman-Lopes A., 2019, MNRAS, 490, 4740
Brook C. B., Kawata D., Gibson B. K., Freeman K. C., 2004, ApJ, 612, 894
Chiba R., Schönrich R., 2021, MNRAS, 505, 2412
Chiba R., Friske J. K. S., Schönrich R., 2021, MNRAS, 500, 4710
Clarke J. P., Wegg C., Gerhard O., Smith L. C., Lucas P. W., Wylie S. M., 2019, MNRAS, 489, 3519
Clutton-Brock M., 1972, Ap&SS, 16, 101
Cunningham E. C. et al., 2020, ApJ, 898, 4
Dehnen W., 2000, AJ, 119, 800
Dierickx M. I. P., Loeb A., 2017, ApJ, 847, 42
Eilers A.-C., Hogg D. W., Rix H.-W., Frankel N., Hunt J. A. S., Fouvry J.-B., Buck T., 2020, ApJ, 900, 186
Fragkoudi F. et al., 2019, MNRAS, 488, 3324
Fujii M. S., Bédorf J., Baba J., Portegies Zwart S., 2019, MNRAS, 482, 1983
Gaia Collaboration, 2016, A&A, 595, A1
Gaia Collaboration, 2018, A&A, 616, A1
Gaia Collaboration, 2021, A&A, 649, A8
Gandhi S. S., Johnston K. V., Hunt J. A. S., Price-Whelan A. M., Laporte C. F. P., Hogg D. W., 2021, preprint (arXiv:2107.03562)
Garavito-Camargo N., Besla G., Laporte C. F. P., Johnston K. V., Gómez F. A., Watkins L. L., 2019, ApJ, 884, 51
Gómez F. A., Minchev I., O'Shea B. W., Beers T. C., Bullock J. S., Purcell C. W., 2013, MNRAS, 429, 159
Gómez F. A., Besla G., Carpintero D. D., Villalobos Á., O'Shea B. W., Bell E. F., 2015, ApJ, 802, 128
Gómez F. A., White S. D. M., Grand R. J. J., Marinacci F., Springel V., Pakmor R., 2017, MNRAS, 465, 3446
Grand R. J. J. et al., 2017, MNRAS, 467, 179
Grand R. J. J. et al., 2021, MNRAS, 507, 4953
Grillmair C. J., 2006, ApJ, 651, L29
Grion Filho D., Johnston K. V., Poggio E., Laporte C. F. P., Drimmel R., D'Onghia E., 2021, MNRAS, 507, 2825
Helmi A., Babusiaux C., Koppelman H. H., Massari D., Veljanoski J., Brown A. G. A., 2018, Nature, 563, 85
Hernquist L., 1990, ApJ, 356, 359
Hunt J. A. S., Bovy J., 2018, MNRAS, 477, 3945
Hunt J. A. S. et al., 2018, MNRAS, 474, 95
Hunt J. A. S., Bub M. W., Bovy J., Mackereth J. T., Trick W. H., Kawata D., 2019, MNRAS, 490, 1026
Hunt J. A. S., Johnston K. V., Pettitt A. R., Cunningham E. C., Kawata D., Hogg D. W., 2020, MNRAS, 497, 818
Kawata D., Baba J., Ciucă I., Cropper M., Grand R. J. J., Hunt J. A. S., Seabroke G., 2018, MNRAS, 479, L108
Kazantzidis S., Zentner A. R., Kravtsov A. V., Bullock J. S., Debattista V. P., 2009, ApJ, 700, 1896
Khanna S. et al., 2019, MNRAS, 489, 4962
Khoperskov S., Di Matteo P., Gerhard O., Katz D., Haywood M., Combes F., Berczik P., Gomez A., 2019, A&A, 622, L6
Kuijken K., Dubinski J., 1995, MNRAS, 277, 1341
Laporte C. F. P., Gómez F. A., Besla G., Johnston K. V., Garavito-Camargo N., 2018a, MNRAS, 473, 1218
Laporte C. F. P., Johnston K. V., Gómez F. A., Garavito-Camargo N., Besla G., 2018b, MNRAS, 481, 286
Laporte C. F. P., Minchev I., Johnston K. V., Gómez F. A., 2019, MNRAS, 485, 3134
Laporte C. F. P., Belokurov V., Koposov S. E., Smith M. C., Hill V., 2020, MNRAS, 492, L61
Laporte C. F. P., Koposov S. E., Belokurov V., 2021, preprint (arXiv:2103.12737)
Li Z.-Y., 2021, ApJ, 911, 107
Minchev I., Quillen A. C., Williams M., Freeman K. C., Nordhaus J., Siebert A., Bienaymé O., 2009, MNRAS, 396, L56
Monari G., Famaey B., Siebert A., Bienaymé O., Ibata R., Wegg C., Gerhard O., 2019, A&A, 632, A107
Noguchi M., 1998, Nature, 392, 253
Pérez-Villegas A., Portail M., Wegg C., Gerhard O., 2017, ApJ, 840, L2
Petersen M. S., Weinberg M. D., Katz N., 2021, preprint (arXiv:2104.14577)
Poggio E., Laporte C. F. P., Johnston K. V., D'Onghia E., Drimmel R., Grion Filho D., 2021, MNRAS, in press
Portail M., Wegg C., Gerhard O., Ness M., 2017, MNRAS, 470, 1233
Price-Whelan A. M., 2017, J. Open Source Softw., 2, 388
Quillen A. C., Dougherty J., Bagley M. B., Minchev I., Comparetta J., 2011, MNRAS, 417, 762
Quinn P. J., Hernquist L., Fullagar D. P., 1993, ApJ, 403, 74
Ramos P., Antoja T., Figueras F., 2018, A&A, 619, A72
Sandage A., Fouts G., 1987, AJ, 93, 74
Sanders J. L., Smith L., Evans N. W., 2019, MNRAS, 488, 4552
Schönrich R., Binney J., 2009, MNRAS, 399, 1145
Sellwood J. A., Nelson R. W., Tremaine S., 1998, ApJ, 506, 590
Toomre A., 1964, ApJ, 139, 1217
Trick W. H., Fragkoudi F., Hunt J. A. S., Mackereth J. T., White S. D. M., 2021, MNRAS, 500, 2645
Vasiliev E., 2019, MNRAS, 482, 1525
Vasiliev E., Belokurov V., 2020, MNRAS, 497, 4162
Vasiliev E., Belokurov V., Erkal D., 2021, MNRAS, 501, 2279
Weinberg M. D., 1999, AJ, 117, 629
Widrow L. M., Dubinski J., 2005, ApJ, 631, 838
Widrow L. M., Barber J., Chequers M. H., Cheng E., 2014, MNRAS, 440, 1971

This paper has been typeset from a TEX/LATEX file prepared by the author.